Received: 1 October 2025 | Revised: 27 December 2025 | Accepted: 3 January 2026

DOI: 10.1002/VIW.20250173

VIEW

RESEARCH ARTICLE

# Quantitative micro-XRF combined with X-ray imaging reveals correlations between Zn concentration and dentin tubule porosity across entire teeth

**Ioanna Mantouvalou**[1,2] | **Leona Johanna Bauer**[1,2] | **Vinh-Binh Truong**[2] | **Yannick Wagener**[2] | **Frank Förste**[2] | **Oleksandra Marushchenko**[1] | **Stephan Werner**[3] | **Franco Lizzi**[4] | **Frank Wieder**[5] | **Timo Wolff**[6] | **Birgit Kanngießer**[1,2] | **Paul Zaslansky**[4]

[1]SyncLab, Helmholtz-Zentrum Berlin für Materialien und Energie GmbH, Berlin, Germany

[2]Institute for Physics and Astronomy, Technische Universität Berlin, Berlin, Germany

[3]Department of X-ray Microscopy, Helmholtz-Zentrum Berlin für Materialien und Energie GmbH, Berlin, Germany

[4]Department of Operative, Preventive and Pediatric Dentistry, Charité—Universitätsmedizin Berlin, Berlin, Germany

[5]Division of X-ray Imaging, Bundesanstalt für Materialforschung und Prüfung, Berlin, Germany

[6]Bruker Nano GmbH, Berlin, Germany

**Correspondence**
Ioanna Mantouvalou, Department of SyncLab, Helmholtz-Zentrum Berlin für Materialien und Energie GmbH, Berlin, Germany.
Email: Ioanna.mantouvalou@helmholtz-berlin.de

**Present address**
Vinh-Binh Truong, Physikalisch-Technische Bundesanstalt, Berlin, Germany
Frank Wieder, Helmholtz-Zentrum Berlin für Materialien und Energie GmbH, Berlin, Germany

**Funding information**
Deutsche Forschungsgemeinschaft, Grant/Award Numbers: 443841418, 396127899

## Abstract

Bony materials are biogenic composites of protein fibers and mineral that create hierarchical structures. In the case of teeth, dentin is the main component and similar to other bones, it contains porosity at multiple length scales. It is traversed by micron-sized hollow channels known as dentinal tubules, essential for temperature and pain sensation. Tubule density and thus porosity vary throughout the macroscopic three-dimensional (3D) structure, with porosity increasing toward the pulp. The different densities in teeth are easily revealed non-destructively in 3D by X-ray imaging using computer tomography (CT). Yet elemental composition analysis is more difficult to obtain from within the centimeter-sized heterogeneous bulk material. We describe an approach of merging CT measurements of healthy, intact bovine teeth with micro-X-ray fluorescence (micro-XRF) images of matching serially sectioned slices. Through the combination of multi-resolution quantitative CT measurements with elemental mass fraction derivation, gradients in density and element distributions such as calcium (Ca), phosphorus (P), and zinc (Zn) are revealed across entire teeth in 3D. While the main constituents (Ca and P) are homogeneously distributed in the matrix, Zn concentration increases significantly and exponentially toward

the pulp. We find an inverse association between dentin tissue density and Zn concentration localizing this element in or around tubules. Our data serve as a quantitative reference for density and Zn mass fractions in healthy, neither carious nor hypermineralized dentin, as a basis for comparisons across species in health and disease states.

**KEYWORDS**
dentin density, micro-computer tomography, quantitative micro-X-ray fluorescence, tubule porosity, Zn distribution

## 1 | INTRODUCTION

All vertebrates (including mammals) possess an "endoskeleton" that is made of the material bone, a biocomposite of collagen fibers and apatite nanocrystals. This material has been the focus of research for centuries (see Reznikov et al.[1]), in particular ever since the discovery of X-rays almost 150 years back. The geometry and characteristics of bone materials remain of high interest not only because of the central role of the skeleton in human health and disease but also for engineers: they serve as bioinspiration for robust, hierarchically organized[2] naturally grown structures that can adapt and change over time. While macroscopically the mineralized fiber composite matrix supports mechanical tasks of the skeleton (e.g., defense), internally it contains water and biological components (enzymes and cells) within a myriad of cavities that are characteristic to different bony tissues.[3] Indeed, the porosity of bony materials, be it macroscopic (e.g., large marrow or tissue spaces), microscopic (blood or cell spaces), or nanoscale (sub-microscopic voids between collagen fiber bundles[1]), is possibly as important for the normal function of the skeleton (mechanical properties and adaptation) as the mineralized matrix is. For example, bones serve as biochemical reservoirs and they house the blood marrow. Many bones are osteocytic, that is, they contain osteocyte cells in the matrix, interconnected by the so-called osteocyte lacuna–canalicular network. The resulting porous network of such osteocytic bones enables mechano-sensation and matrix turnover, both central to the adaptive response of bones to load or damage. However, a significant number of bony materials do not contain osteocytes. Consequently, the design principles as well as the natural mechanisms of damage resistance and deformation response are the subject of ongoing investigations.[4–6] Dentin is one example of a bony material that is characteristic of vertebrate teeth.[7] In mammals, dentin shapes the roots that are anchored to the jawbones, while forming dome-like hollow structures that define tooth geometry and support enamel in the crown. Dentin is known for strength and toughness,[8,9] required for decades of tooth function without failure. Yet dentin lacks osteocyte cells and the capacity for tissue turnover or replacement even though it is highly porous due to the presence of micron-sized hollow channels known as dentinal tubules. These cavities traverse the entire dentin thickness, leading from the pulp tissue in the root/pulp chambers outward, to the tooth periphery. As early as 1976, Garberoglio and Brännström[10] showed that, in human teeth, the dentinal tubules are denser and wider near the pulp. Indeed, in normal healthy mammalian dentin, tubules become thinner and more dispersed at increasing distances outward, toward the external tooth surfaces.

The tubule porosity makes it possible for liquid to flow through dentin and to come into contact with odontoblasts, dentin forming cells, situated at the border between the pulp tissue and dentin.[11] Odontoblasts are thus not normally found buried inside the dentin matrix bulk, rather they reside in the pulp chamber. They are the cells responsible for the material creation during odontogenesis, which they do by creating pre-dentin that subsequently mineralizes. The process is similar to osteoid in bone, where the material is produced by osteoblast cells.[12] One important difference is that odontoblasts retain a tight contact to the dentin matrix that they created in the form of elongated finger-like cellular remnants, known as "odontoblast processes," that are left within many dentinal tubules during dentin deposition.[13]

Based on these structural observations, it may be understood that dentin porosity is not uniform because it varies in different tooth regions. The porosity of dentin has been indirectly assessed by measuring the "hydraulic conductance" in cross-sections of teeth. This a parameter is useful to quantify flow across dentin, for example, of bacteria.[14] More recently, it was shown how permeability can also be derived through calculations based on synchrotron micro-CT data.[15] It is also a measure of the permeability, important for dental treatments such as bonding of biomaterials used for fillings.[16,17] In living ("vital") teeth, the tubule-mediated porosity plays an important role in

tooth pain sensation, enabling rapid liquid flow through tubules,[18] that may be converted into sensation via free nerve endings[19] or other odontoblast responses.[20]

One consequence of the varying porosity is that the density of the tissue (dentin "tissue density") is also not constant—as opposed to the "matrix density," relating specifically to the mineralized fiber matrix surrounding the tubule voids. In bony tissues, tissue density is correlated to tissue stiffness[21] (although not strength[3]). This is of significance also in teeth, where laboratory-based micro-computer tomography (micro-CT) measurements have demonstrated reduced absorption and lower tissue density near the pulp,[22] which explains the reduced hardness in this area.[8] The signals that micro-CT measures are the product of the matrix density of the material diluted by the presence of internal voids that may actually be smaller than the resolution of the measurement. Because of physical constraints in resolution and flux, laboratory measurements of dentin by micro-CT frequently cannot resolve the micron-sized tubules. Under the assumption that the composition and density of the dentin matrix surrounding tubules is more-or-less constant, the gray values of tomography measurements are—to a first approximation—reciprocal to the tubule porosity. Therefore higher micro-CT densities correspond to lower hydraulic conductance.

Chemically, and just like all other bony materials, the dentin matrix is made of non-stochiometric carbonated apatite nanocrystals [$\sim Ca_5\{(PO_4)_{0.75}(CO_3)_{0.25}\}_3(OH)$] and organic polymers, mainly collagen ($\sim C_{65}H_{102}N_{18}O_{21}$). Thus, the elements Ca and P in the nanocrystals are the main heavy elements (with atomic numbers greater than 14) present, although some Zn has been reported, alongside S.[23] Light elements such as Mg as well as traces of F and Na are also found within the dentin composite matrix. With regards to Zn, early publications of its distribution in human dentin date back to the work of by Brudevold et al. in 1963.[24] They showed high concentrations of this element in outer enamel and they demonstrated a gradual increase of Zn in dentin toward the pulp chamber. Similar trends and increased Zn near the pulp were reported in a range of mammals,[22,25] including marsupials.[26] Thus, in normal, untreated tooth dentin, an increase in Zn concentration in the bulk material is expected to be found toward the pulp of healthy teeth, though not always reported.[27] Yet, at the micron level, the composition of dentin in regard to Zn has not been systematically quantified across entire intact teeth, to the best of our knowledge.

The increased Zn concentration and increased tubule porosity in dentin near the pulp raise the possibility that these phenomena are associated with one another, at least in natural, healthy, fully mineralized teeth. However, the presence of spatially varying porosity poses an experimental challenge when trying to quantify variations in chemical composition which is also related to the tissue density. Chemical composition of materials is usually measured on exposed surfaces that can easily be analyzed directly by high-resolution characterization methods such as scanning electron microscopy coupled with energy-dispersive spectroscopy (SEM–EDX). However, such methods cannot reliably measure the bulk below the surface, as the chemical signal of EDX is limited to excitation of the upper ~1 μm of the material. X-ray methods are needed to extend this information into the full three dimensions (3D), especially because electron microscopy imaging of entire crowns and roots is usually not feasible. X-ray methods of imaging and chemical mapping are of high relevance, since X-rays can penetrate deep into bony materials, including teeth, and they can be easily adapted to measure and quantify gradients within centimeter-sized dimensions, which is typical of teeth.

Specifically, micro-X-ray fluorescence (micro-XRF) spectroscopy is a quantitative non-destructive elemental imaging technique, which relies on the detection of XRF following excitation with a focused X-ray beam.[28] The technique demands no specific sample preparation and can deliver elemental information emerging through hundreds of micrometers of material found deep in the bulk of composites, such as dentin, due to the propagation of the excited X-rays.[29] The information depth (the depth from which 1/e of the emitted fluorescence photons originate from) is density, energy—and consequently—element-specific. For example, in dentin, the signal detected for Ca arises from a depth of up to ~30 μm (for K-radiation emission lines) whereas the signal for Zn (K-radiation) emerges from depths of up to ~100 μm.[29] The XRF intensity of an element corresponds to its concentration, but the relationship is not the same for all elements. This is due to self-absorption as well as factors such as polychromatic excitation and the different fundamental parameters governing the fluorescence emission processes for each element. Overall, the relationship between XRF intensity and concentration of an element can be calculated with the Sherman equation[30]—a set of coupled non-linear equations—which allow for a full quantification, if the instrument and sample parameters are well known. In contrast to SEM–EDX, XRF spectroscopy is highly sensitive to elements with atomic numbers higher than 20,[31] facilitating the imaging of Zn even in composites comprising low ppm concentrations.

Here, we tackle the challenge of quantifying elemental distributions, in particular of Zn, in the bony material dentin, taking into consideration the varying tubule density. We show the coupling of complementary X-ray imaging methods with chemical mapping of fully mineralized tooth dentin. The merging of data from CT and

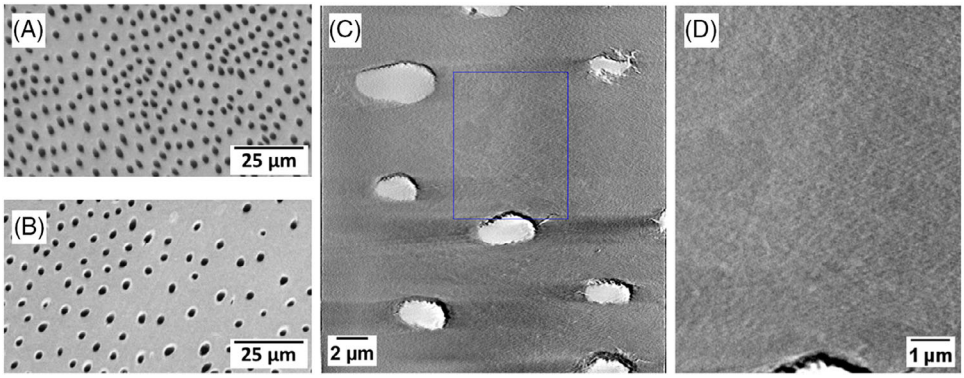


**FIGURE 1** (A and B) High-magnification backscattered scanning electron microscopy (BSE–SEM) images collected from a polished bovine tooth slice, imaged both near the pulp and 1 mm away, respectively. Tubules appear as dark hollow voids. In (B) many tubules are surrounded by bright rings of high-density peritubular dentin (PTD). (C) Reconstructed virtual slice of a 1 µm thick dentin lamella, milled within a normal tooth by means of a focused ion-beam (FIB), imaged tomographically by X-ray transmission microscopy. (D) A higher magnification image of intertubular dentin (ITD) in the area marked in blue in (C) shows traces of the mineralized collagen fibers of ITD, observed at nanometer resolution between tubules.

micro-XRF results in a detailed 3D picture of the main structural gradients of dentin, as observed in healthy intact teeth. Our approach makes it possible to quantify gradients and investigate the association between natural porosity and physiological Zn gradients within macroscopic volumes of tooth material, which may serve to understand the roles and dynamics of Zn in various mineralizing tissues.

## 2 | RESULTS

Figure 1 shows typical example backscattered scanning electron microscopy images of cut and polished bovine dentin, revealing exposed tubules near the pulp (Figure 1A) as well as approximately 1 mm outward (Figure 1B). Such images in a healthy neither carious nor hypermineralized bovine molar demonstrate the increase in tubule porosity observed in the matrix near the pulp. Due to differences in the electron backscatter signal, tubules appear as dark hollow voids within the mineralized dentin matrix ("intertubular dentin"—ITD). In crown dentin, about half-way between the pulp and enamel, many tubules become surrounded with a normal yet hypermineralized peritubular sheath[32,33] ("peritubular dentin"—PTD) that leads to a small increase in the mean tissue density.[34]

Dentin tissue imaged by transmission X-ray microscopy (TXM) tomography reveals, at nanometer resolution and in 3D, the fibrous nature of the ITD matrix. Figure 1C shows a reconstructed slice within a 1 µm thick lamella (sized 14 µm × 17 µm in lateral dimensions) extracted ~90 µm away from the pulp (see Supporting Information, Section 1, for details). At such proximity to the pulp, no PTD is present, and the more-or-less uniform matrix density of the ITD is revealed, as demonstrated by a close-up image of the matrix located between neighboring tubules (Figure 1D), in which traces of the mineralized collagen fibers are visible.

While electron and TXM provide insightful high-resolution results, they are restricted to very local fields of view thus of limit in revealing gradients in dentin tissue density across large millimeter–centimeter-sized samples. For such larger length scales, commercial laboratory micro-CT instruments provide 3D data with reasonable high spatial resolutions. Figure 2A depicts a 3D rendering of typical micro-CT data of one of several bovine teeth (T4) with a second rendering showing the same data with a virtual cutout that makes it possible to examine the internal pulp chamber surrounded by dentin. Slices along this tooth (e.g., panel c) reveal characteristics of such samples: the uppermost image demonstrates tissue density variations in an example slice in the micro-CT data (gray value units). The virtual cut reveals high absorption in enamel (the diagonal upper right-side feature) and a moderate gradient in tissue density (brightness) in dentin, observed when exploring the image information from the pulp in the center, outward toward the external tooth surfaces (periphery). The three lower figure panels show the results of micro-XRF mapping of the corresponding physical slice in this tooth, revealing the K-line intensities of the elements Ca, P, and Zn. Whereas the micro-CT data represents the tissue density in a 24 µm thick (virtual) slice in the tomography data, the micro-XRF information originates from different depths beneath the physically cut and polished tooth slice surface. The XRF signal for P and Ca (emerging from a thickness of up to 30 µm) is emitted from the mineral component of the dentin matrix, emerging from the same volume imaged by micro-CT. This is

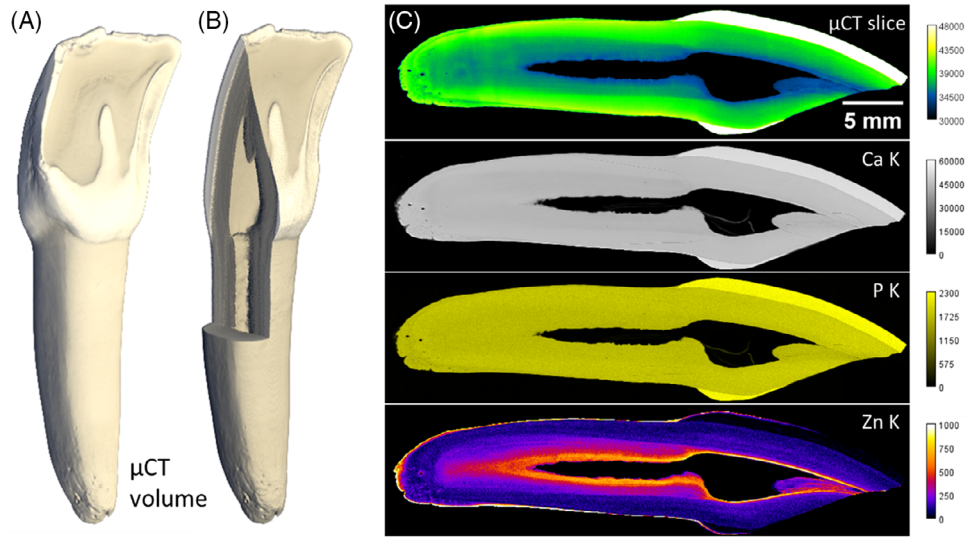


**FIGURE 2** Comparisons of micro-X-ray fluorescence (XRF) and micro-computed tomography (CT) data; micro-CT rendering of a full tooth (T4) (A) with virtual cutout exposing variable densities and internal structures (B). (C) Micro-CT slice of the same volume showing the absorption in gray value units. Beneath it, the P, Ca, and Zn K-line fluorescence intensity distributions of a physical cut slice are shown. Fluorescence intensity values are given in counts per second (CPS), higher counts to a first approximation correlate with higher concentrations of the heavier elements.

because the excited XRF radiation for these elements is only detectable from rather shallow dentin layers, tens of micrometer deep. The Zn K fluorescence however originates from greater depths beneath the slice surface (up to ~100 µm). The Ca and P K-line fluorescence intensities are high, corresponding to a strong signal from the high-prevalence dentin mineral, and both elements appear to be relatively homogeneous across dentin (with even higher intensities observed in enamel). Notably, the Ca to P ratio does not change in different dentin regions, suggesting a uniform composition of the apatite crystal stoichiometry in the mineralized collagen matrix. In contrast, the Zn signal is strongly enhanced toward the pulp. To that end, and even though mineral (Ca and P) is the main cause for absorption, it is curious to observe how none of the chemical maps mirrors the absorption distribution seen in the micro-CT (panel a) data. Close examination suggests that the Zn signal may be inversely proportional to the absorption revealed by the micro-CT data.

Micro-XRF measurements of multiple slices from root and crown regions of several teeth (T1-T3), show similar results. The Zn maps reveal a recurring pattern of an increase in Zn signal in dentin near the pulp. We used point-by-point XRF measurements to generate mean spectra (see Figure S2) of all areas with similar Zn K-line intensities in layers with increasing distances from the pulp (Figure 3A). These spectra yield information from which it is possible to quantify the mass fractions of the main elements, Ca and P as well as the trace Zn using a software package based on the Sherman equation.[30] During quantification, the "dark matrix," made of all elements which are not directly detected in the XRF spectrum, is taken into consideration. It typically includes light elements such as C, N, and O where fluorescence detection is difficult due to extensive self-absorption and low fluorescence yield. As a result, quantitative mass fractions for all investigated spectra can be extracted with a 10% uncertainty, as described in detail in Section 6.

The results of the quantification can be plotted on a topological scale from the pulp region to the outermost periphery (plotted in six steps due to the six averaged spectra per slice). As shown in Figure 3B, the results demonstrate a high similarity observed between different teeth. Plotting the data in this manner makes it easy to compare the Ca and P distributions between different crown and root slices: it becomes apparent that the crowns and roots of different young healthy teeth are visibly very similar. Specifically, the major apatite mineral elements Ca and P mass fraction values differ only mildly at different distances to the pulp. This is surprising, because the micro-CT data clearly show that the near-pulp regions have a lower tissue density. To understand this, it is necessary to recall that the information depth for XRF signals emitted by Ca and P is restricted, due to self-absorption by the tooth matter. The signal thus arises mostly from near-surface areas (~30 and ~10 µm beneath the tooth slice surface,[29] respectively). Within such thin layers there can only be a couple of tubules, so that variations in tubule density have negligible effects on the average detected Ca and P signals emitted by the more-or-less homogeneous matrix.

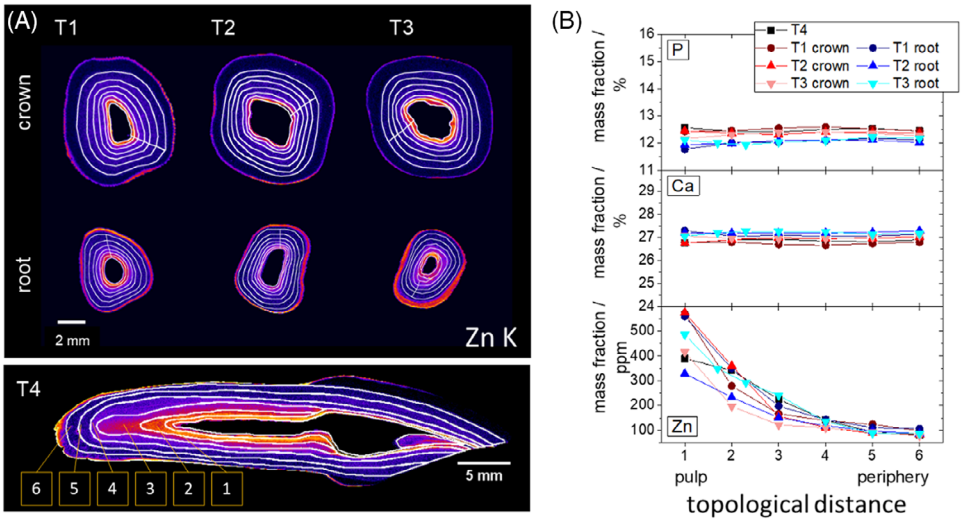


**FIGURE 3** (A) Topological maps of the Zn K intensity used for the generation of mean spectra (white lines separating the six areas). (B) Mass fraction values for Ca, P, and Zn as a function of the topological distance defined in (A) derived through quantification of the mean spectra by means of the Sherman equations.

In contrast, the Zn mass fractions (with the XRF signal arising from an information depth of ~100 μm[29]) show a marked gradient across the tooth thickness. Our quantification reveals a 10-fold increase in Zn concentration from about 50 ppm in peripheral dentin regions, increasing up to 500 ppm near the pulp. This trend is independent of the tooth or the location of the slice in the tooth, and recurred in all our analyzed slices.

The quantitative XRF results make it possible to establish the relationship between Zn K intensity and Zn mass fraction. While this relationship is generally complex due to self-absorption, scattering and secondary effects, in the limited parameter space here, where the density and matrix of the sample do not change significantly, a linear description can be used to a first approximation. Using this linear dependency, the measured micro-XRF intensity images of the slices were converted into mass fraction maps, yielding fully quantitative images of chemical composition of the different slices as presented in the bottom images of Figure 4A.

The absolute tissue density values for the same tooth slices were obtained by measuring calibration samples together with high resolution micro-CT measurements of the entire cut slices. For this purpose, calibrated (tissue density-determined) reference samples of dentin and enamel were prepared from a fifth tooth. A linear calibration curve utilizing dentin, enamel and the known density of supporting glass slides as described in Section 6 facilitated the generation of quantitative images of tissue density (top images of Figure 4A). Both calibration curves (for Zn and tissue density) are shown in Figure S3.

Figure 4 compares slices across three teeth (crown and root) and shows averages of five virtual slices of cross-sections in the calibrated micro-CT data. These are displayed along with the quantitative Zn distribution maps obtained from the corresponding physical slices. Whereas the dentin tissue density values span 1.75–2 g/cm$^3$ the Zn mass fractions occupy a range between 50 and 500 ppm. Both tissue density and mass fraction values display predominantly radial patterns with increasing tissue density and decreasing Zn values observed at increasing distances from the pulp toward the tooth periphery.

In each of the slices, four example line profiles clearly demonstrate the trends (positions marked with yellow lines, one roughly horizontal and one vertical, Figure 4A). Figure 4B shows the tissue density (top) and Zn mass fraction (bottom) of the four corresponding profiles for the T1 crown slice, plotted against distance to the pulp. Both the tissue density curves as well as the Zn mass fractions can be described with an exponential dependency as a function of the distance to the pulp [fit = area × exp(– exponent × distance) + offset].

Interestingly, in some of the dentin regions in particular near the pulp, circumferential increases in tissue density can be discerned (e.g., T3 crown). When imaging these regions with SEM, these regions correspond to regions of blocked tubules attributable to dentin sclerosis[35] (see Figure 5). Such patterning is not visible in the Zn mass fraction images suggesting that the radial Zn distribution is inherent to the tooth formation with no direct association to later tubule mineralization processes taking place due to attrition or infection.

The boxplots in Figure 6A,B summarize the exponential fit parameters from all the cross-sectional slices of T1, T2, and T3. An exponential decrease of tissue density is observed toward the pulp but this varies considerably.

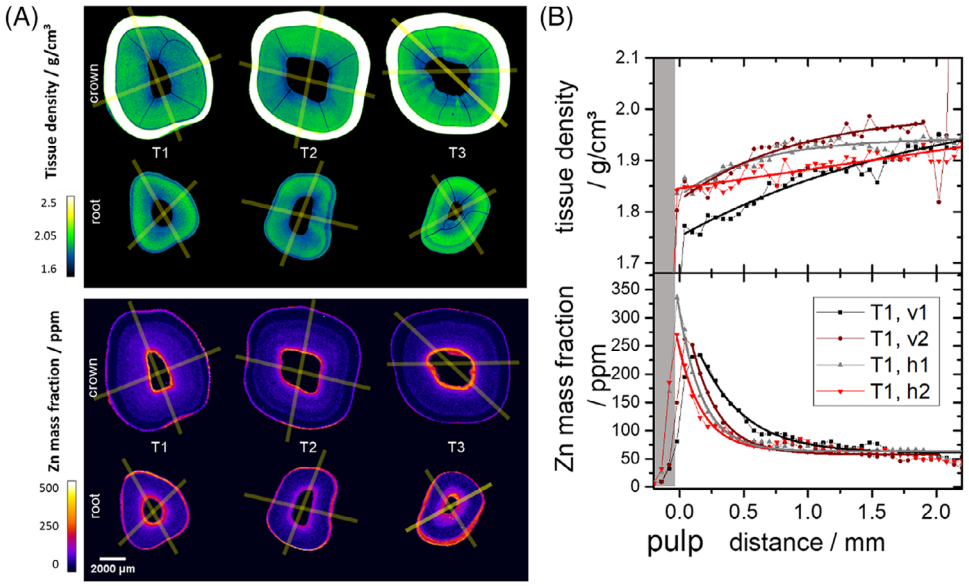


**FIGURE 4** (A) Quantitative Zn mass fraction and tissue density images of six selected slices in teeth T1–T3. Zn mass fraction and tissue density appear to be inversed. From each slice, two line profiles (roughly vertical [v] and horizontal [h]) were used to plot profiles as shown in panel (B) (300 µm thick line average). (B) Example line profiles from the crown slice of T1 show tissue density (top) and Zn mass fraction (bottom) as a function of distance to the pulp (marked in gray). Enamel (in the crowns) and cementum (in root slices) are excluded from the fitting, to focus on the trends within dentin. The Zn mass fraction profiles and tissue density profiles are fitted with exponential functions (bold lines) (T1, v1: tooth 1, vertical/horizontal profile 1/2, values from the first/second half of each profile).

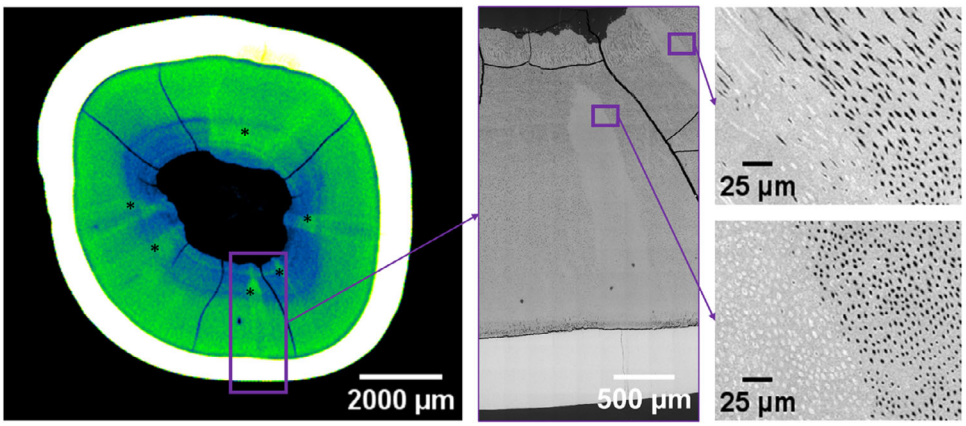


**FIGURE 5** Computed tomography image of the crown slide of T3. Density variations can be seen (marked with stars). This slice was imaged with a scanning elctron microscopy (SEM) instrument to investigate the regions with higher tissue density. The high-resolution images clearly show blocked tubules, typically associated with dentin sclerosis.

There is a slightly higher mean exponent for the crown data. Additionally, the crown data show a higher variance which could be explained by the frequent observations of PTD or tubule blockage (see Figure 5). For the Zn mass fractions, the exponential behavior is distinctive with a faster increase in the crowns compared to the root cross-sections, as seen by the lower exponents observed in the root fits. In Figure 6C,D, the tissue density is plotted against the Zn mass fractions separately for the crown and root slices. A base (minimum) level of about 50 ppm of Zn is found for mature dentin (across multiple teeth), in the same areas where we consistently observe a tissue density of about 2 g/cm$^3$. Wherever the tissue density decreases, Zn mass fractions increase, with the lower tissue density dentin regions near the pulp exceeding Zn values of 300 ppm. The graphs suggest an exponential behavior for the dependency between Zn mass fraction and tissue density.

The 2D maps of Zn ($n = 32$ cross-sections and $n = 14$ longitudinal slices of teeth T1 and T4, respectively) were correlated in 3D with the CT data obtained initially of the intact teeth using suitable segmentation procedures and a simple

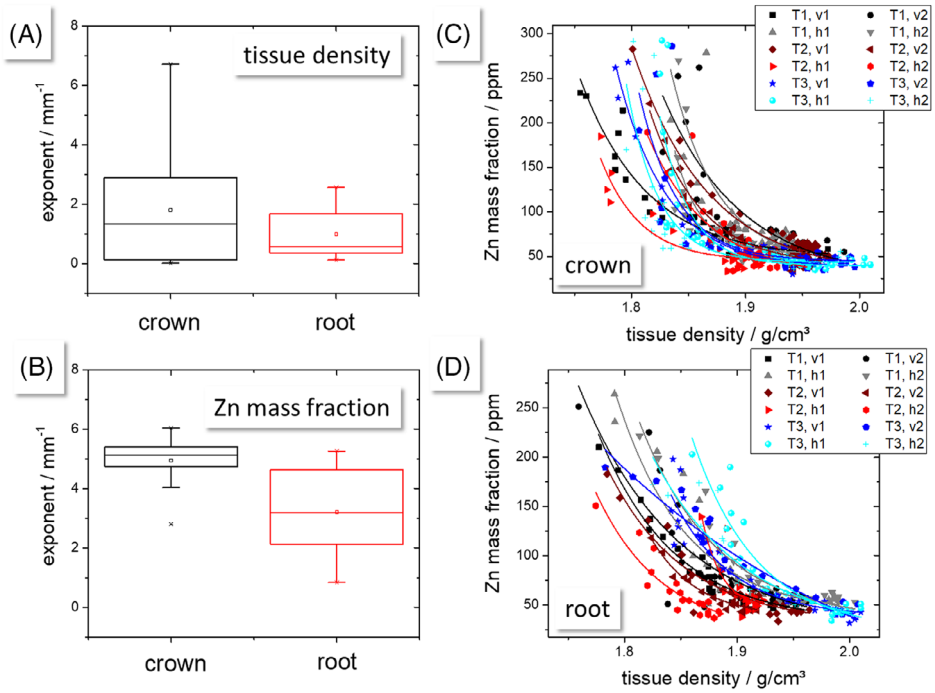


**FIGURE 6** (A) Box plot of all exponents extracted from the tissue density line profiles of all slices in Figure 4A. The decrease of tissue density is slightly different between root and crown, with a wide spread in curve shapes. (B) Box plot of the exponential fits of the Zn mass fraction as a function of distance to the pulp. A statistically significant difference between crown and root can be seen. (C and D) Zn mass fractions are plotted against the tissue density for crown and root data, separately, and fitted with exponential functions (T1, v1: tooth *x*, vertical/horizontal profile 1/2, values from the first/second half of each profile).

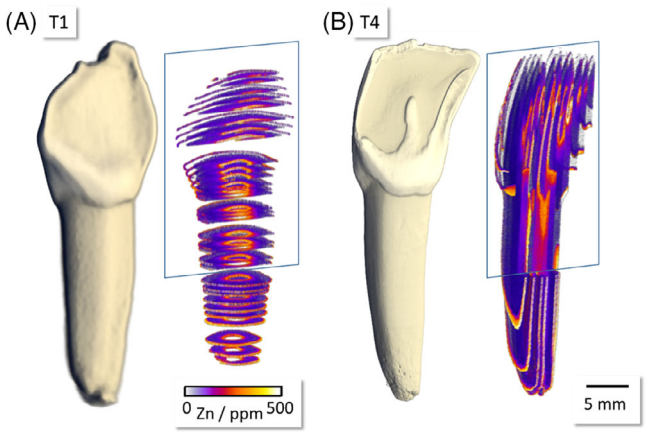


**FIGURE 7** Three-dimensional (3D) representation: chemical picture in 3D of two teeth, one cut using cross-sections (T1, A) and one longitudinally (T4, B). The micro-computed tomography (CT) renderings (left) show the intact teeth and the Zn data (false color images, right) is virtually cut open (blue rectangles) to demonstrate the full information in 3D.

template-matching algorithm, see Section 6 and Supporting Information for details. The matched data sets allow us to co-align and visualize the distribution of all measured elements in 3D, see also the video of T4 in the Supporting Information. The results are shown in Figure 7 depicting the 3D Zn distribution in false colors with a virtual cutout to demonstrate the internal distribution of the elements.

## 3 | DISCUSSION

Our work reveals opposite trends in the Zn concentration and in the local dentin tissue density by merging complementary X-ray measurements from tomography with XRF elemental mapping at the micrometer length scale. The result is a quantitative description of the normal, physiological Zn distributions in the crowns and roots of teeth with healthy dentin, with no effects of caries or extensive hypermineralization. An immediate observation (see Figure 6) is that increased Zn concentration does not contribute significantly to the dentin tissue density (which decreases whenever we observe higher Zn concentration).

With increasing proximity to the pulp, we observe a moderate, exponential decrease in the tissue density while at the same time, we reveal a pronounced exponential increase in the Zn mass fraction. We find this to be the case in all the healthy, fully formed (~4 years old) teeth tested. Importantly, this appears to be characteristic of mammalian dentin, and therefore it is not a surprise that we find this also in bovine teeth, a model system frequently used in dental research.[36] Therefore this Zn enrichment

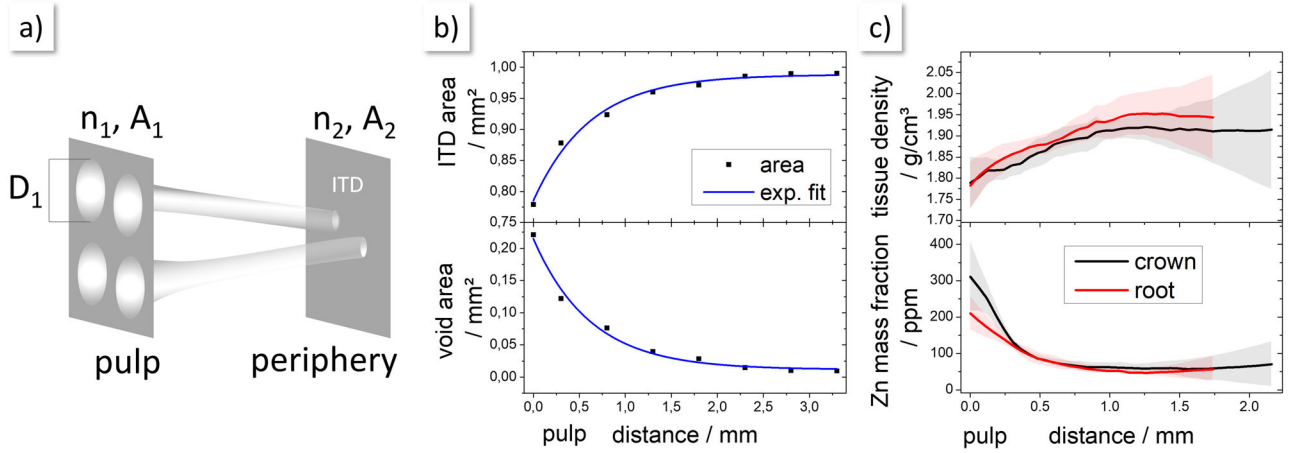


**FIGURE 8** (A) Simplified schematic representation of changes in number and area of tubules in dentin. (B) Dentin and void area calculated with the values from Garberoglio and Brännström[10] and Equation (1). (C) Averaged line profile values of the tissue density and the Zn mass fraction determined in our work for the crown and root profiles (Figures 4 and 6), the standard deviation uncertainty is plotted as shaded regions.

near the pulp represents the normal chemical composition, and the gradient we quantify is the tissue norm. There appears to be an association with increased tubule porosity (inversed to dentin tissue density) and therefore Zn might be preferentially localized to tubules around the pulp of mammalian teeth. To understand our results, we consider a simple model that integrates known measurements of the dentin composite structure and porosity. The model considers a surface inside dentin, oriented perpendicular to the tubules. In a representative cross-sectional area $A_i$ tubules become larger at increasing proximity to the pulp. In any such cross-section, the area occupied by tubules $A_{T,i}$ increases as a function of the number of tubules $n_i$ as well as the tubule diameter $D_i$ (see Figure 8A). The ITD (corresponding only to the dentin matrix material) area $A_D$ can therefore be described by

$$A_D = A_i - A_{T,i} = A_i - n_i \frac{\pi}{4} {D_i}^2. \quad (1)$$

Considering the values published by Garberoglio and Brännström[10] the void and tubule cross-sectional areas can be estimated (see Figure 8B). We find that as the ITD area decreases, the void area increases.

Measured independently by our XRF methods, we find an exponential increase in the Zn mass fraction in dentin tissue nearing the pulp (Figure 4). Specifically, there is a 5–10-fold increase in Zn concentration within 1 mm distance to the pulp chamber, where a mass fraction of up to 500 ppm is found at the transition between dentin and the pulp tissue. On the opposite, outer rims of the teeth sections, the Zn mass fraction is the lowest, ca. 50 ppm observed far from the pulp. In such peripheral areas, tubule density and diameters are the lowest. When comparing the exponential increase of the Zn mass fraction to the tubule porosity in Figure 8B a tight association is observed. This observation makes it possible to speculate on where the Zn elements are localized in the tissue.

There have been proposals that Zn is incorporated into the nanocrystals of hydroxyapatite, substituting for Ca in the crystal structure.[24,37] While the increase of Zn that we observe toward the pulp is substantial, the absolute amount in comparison to the dominant Ca concentration is very small (compare 50 –500 ppm for Zn to 27% for Ca). Therefore, neither the Ca to P ratio nor the *c*-lattice parameter is expected to change significantly with the increase in Zn concentration. Indeed, microbeam X-ray diffraction (micro-XRD) line profiles in 200 μm thick samples of bovine root sections (Figure S4), annealed to release any collagen compression effects on the nanocrystals,[38] reveal no significant change in the crystal lattice in the regions showing strong Zn concentration increase. Line profiles from the external cementum all the way to the pulp reveal some crystal lattice decrease only up to about 1 mm from the pulp (see details in the Supporting Information). In other words, the regions in dentin where tissue density decreases and Zn concentration increases near the pulp are the same areas where the *c*-lattice parameter is rather constant, suggesting that the Zn concentration in dentin does not change the apatite lattice parameter. Other crystal inclusions such as $CO_3^{2-}$ substitution[39–41] are more likely to be the cause of *c*-lattice deformations in dentin apatite nanocrystals. Therefore, we propose that Zn near the pulp is not significantly incorporated into the apatite nanocrystals of native, healthy mammalian dentin.

Our results suggest that it is more likely that Zn resides in a different habit in teeth, taking into account that several literature studies[22,42] report that Zn is embedded

within the organic matrix as a key component of enzymes such as matrix metalloprotease (MMP) or alkaline phosphatase (ALP). This observation matches findings by other authors, for example, Stock et al.[22,43] who used nanometer-sized XRF beams to show Zn enhancement in bovine teeth around tubules. Those authors proposed that Zn enhancement was related to PTD, although they did not show this. It is well known in fact that PTD is mainly found in mid-crown regions[44] and not near the pulp. Our data show that the increase in Zn concentration near the pulp is seen for both crown and root dentin. This suggests that it is organic material in or around the tubules that harbors Zn not the PTD. Indeed, the increase in Zn in the near-tubular dentin may be a remnant or indirect trace of the mineralizing front for both PTD or ITD.[22] Since Zn has been associated with mineralization fronts,[45] possibly concentrated in ALP enzymes,[42,46] the higher concentration of Zn raises the possibility that some enzymes may become entrapped in the ITD surrounding tubules, as the tissue mineralizes.

We find that the average dentin tissue density in all our quantified tooth slices decreases at increased proximity to the pulp, with averagevalues typically spanning 1.8–2 g/cm$^3$. We thus expect tissue density to follow the dentin area as depicted in Figure 8B. Deviations from the exponential dependency likely hint to the presence of PTD or to tubule blockage, as we show for one example slice in Figure 5. Indeed, although we investigate young, healthy teeth, we observe in multiple regions early stages of tubule blockage. Thus, as suggested by others,[45] mineralization and sclerosis of tubules may start early in the life-cycle of teeth in mammals.

Our 3D micro-XRF data, collected from healthy, non-treated relatively young bovine teeth, provide the first quantitative distributions of natural Zn in healthy dentin collected in a series of slices that we used to generate a complete 3D volumetric quantification. The 3D distribution of Zn is showcased in Figure 7 based on different teeth where both longitudinal and cross-sectional slices were measured. The Zn signal in dentin is always strongly (~10-fold) enhanced toward the pulp.

## 4 | LIMITATIONS AND OUTLOOK

Here we focus on only XRF for deriving the Zn quantification because unfortunately, SEM–EDX measurements proved unsuitable to detect the low quantities of Zn present in natural dentin. Further studies are needed for comparison with other (destructive) imaging techniques such as laser ablation inductively coupled plasma mass spectrometry (LA–ICP–MS) to validate and perhaps improve on our results.

Although we are not able to show similar data in young, mature, untreated human teeth (due to ethical restrictions), the findings in bovine teeth highly match and help explain previous reports in samples from patients.[27,45] It is therefore likely that in natural, healthy teeth the Zn is bound to (organic) molecules and is not free to diffuse; hence, it is likely entrapped in the dentin, but Zn might become mobile and possibly chemically reactive, if demineralization takes place (e.g., due to acidic processes such as caries, but perhaps also acid-etching/filling placement). This is different from diffusion of clinically used zinc containing pastes and biomaterials (such as ZnO) placed, for example, during root canal treatment. Such Zn formulations have known bactericidal and anti-pathogenic activity but the ionic stability is different, which we see as being detached from the biological molecules and Zn that comprise the dentin nanocomposite.[43] The relatively high natural concentration of Zn found near the pulp does not seem to prevent caries: in fact, higher concentrations of Zn have been found in carious regions[47–49] that are a significant concern when dentists treat deep cavities, where the fillings are placed near the pulp (i.e., in areas that have high natural Zn content). Here, one may speculate that natural Zn has a possibly negative dental-care effect, as Zn within the natural MMP enzymes may become active to participate in dentin degradation (e.g., collagenases) associated with caries progression, as discussed extensively elsewhere.[45] This may be related in part also to previously reported correlations between dentin permeability (mediated by to porosity) and adhesion of fillings.[17] Our results suggest that the naturally elevated Zn concentrations near the pulp, observed in both the crown and root, may contribute to enzymatic degradation of dental restorative bonding to deep-placed fillings. Further studies in human teeth are needed to confirm this hypothesis. If confirmed, in particular with an increased population of ageing individuals with root exposure and possible deep caries, treatment beyond prevention might require alternative approaches that do not make use of dentin etching, demineralization and release of entrapped Zn (e.g., from MMPs).

## 5 | CONCLUSION

By combination of micro-CT and micro-XRF we were able to generate a quantitative correlation of Zn concentration inside the bulk of healthy dentin tissue of varying densities to reveal the 3D gradients that are typical for the macro-structure of young healthy bovine teeth. Dentin porosity in bovine teeth changes significantly at different distances from the pulp amounting to differences on the order of 10%–20% within regions of tissue that encase the pulp tissue. The composition of the dentin intertubular matrix is more or less homogeneous, the only significant chemical change observed in the natural tissue is the Zn

distribution. We observe an inverse relationship between Zn concentration and tissue density following a seemingly exponential dependency that results in a 5–10-fold increase in Zn near the pulp. This substantial increase is associated with an increase in tubule diameter. If dentin ITD composition is more or less homogeneous in all tooth regions, our findings hint to a possibility that a major source of Zn is from the tissue within tubules, and not the ITD. Possible sources of such Zn might be odontoblast membrane enzymes or various matrix proteases that could localize preferentially in or around tubules, which suggests that very little if any Zn is localized within mineral nanocrystals, as we recently demonstrated for fish-bones.[5] While the present study shows data from bovine teeth, Zn enhancement toward the pulp has been repeatedly reported also in human teeth,[22,24–26] showcasing the usefulness of the abundantly available bovine tooth material as a model that reproducibly simulates human healthy untreated dentin material.

## 6 | EXPERIMENTAL/METHODS

### 6.1 | Bovine tooth samples

Several ($n > 5$) untreated bovine teeth (3–4 years old animals slaughtered for human consumption) were provided by Fleischhandelsgesellschaft Henke, ensuring similar dietary conditions. After extraction and mechanical cleaning, the teeth were stored in 0.5% Chloramine T following standard tooth storage procedures routinely performed at the dental clinic of the Charité Berlin.

### 6.2 | Scanning electron microscopy

Several ($n = 4$) slices were cut across multiple hydrated bovine teeth, after embedded in self-curing dental acrylic (Technovit), see below. Each slice was ground and polished with a series of SiC grinding papers polished up to the finest polishing paper with a grit of 4000. The samples were allowed to slowly dry in air, before imaging in an electron microscope (Phenom-XL, ThermoFisher) under low vacuum (60 Pa) imaging conditions.

### 6.3 | Transmission X-ray microscopy

From one of the slices, several 1 μm thick lamellas were prepared (see description in the Supporting Information). TXM measurements were performed at the U41 TXM Beamline of the synchrotron radiation facility BESSY II operated by the Helmholtz-Zentrum Berlin. At a set energy of 1 keV, 118 radiographs at angles between –60° and +57°, were collected with a step size of 1°and 4 s exposure time at a magnification of 1449×. Subsequently, 10 flat field images were measured.

For reconstruction, Fiji/ImageJ with different plugins was used. A flat-field normalization was performed using the minimum standard deviation method. With the TomoJ plugin,[50] the stack of radiographs was first aligned. Then, phase retrieval was performed with the ANKAphase plugin[51] ($\delta/\beta = 6.45$, distance = 0.0000002667, pixel size = 0.02 μm) and, finally, reconstruction was performed again with the TomoJ plugin (iterative/art/25 iterations/0.2 relaxation coefficient/fista optimisation is on).

### 6.4 | Computer tomography

For imaging of intact teeth, 3D data were collected prior to drying. T1–T3 were measured with a medical cone beam CT setup (Veraviewepocs 3D R100, J. MORITA EUROPE) which utilizes a rotating X-ray source and detector system for patient treatment. The X-ray source was set to 75 kV and 10 mA and a 0.2 mm Cu filter was used. With total exposure times of 9.3 s, the scans resulted in CT images with 125 $\mu m^3$ isotropic voxels. Standard settings were used as defined by the manufacturer, and the data were reconstructed using the Morita inbuilt control and reconstruction software.

For tooth T4, an industrial micro-CT setup (Xradia 620 Versa, ZEISS at BAM) was used. The X-ray cone beam was set to 90 kV and 0.1 mA. To reduce effects of beam hardening, a filter was used to absorb the softer X-rays, situated directly after the source beam window. Data (2400 projections) yielded a tomographic dataset with a voxel size of 24 $\mu m^3$, reconstructed with the standard Zeiss reconstruction pipeline using the filtered-back-projection method.

### 6.5 | Mechanical sample preparation (T1–T4 + references)

The teeth were dried in a sequence of increasing ratios of alcohol-water solutions (70, 80, 90, and 100% alc.), for gentle dehydration.[52] Subsequently, the teeth were embedded in Technovit 7200 VLC and light-cured (EXAKT 520, EXAKT Advanced Technologies GmbH), placed in an oven at 40°C to complete the hardening. The embedded teeth were sliced using a water-cooled diamond band saw (EXAKT 310) to produce slices of a thickness of approximately 200 μm. Three of the bovine teeth were cut horizontally (T1–T3), resulting in 33, 36, and 39 slices, respectively, while the fourth bovine tooth (T4) was cut longitudinally, resulting in 18 slices. Each slice was mounted on a plexiglass slide (Walter Messner GmbH). The thickness and density of these slides were measured before the sample preparation. The tooth slices were subsequently polished using a microgrinder (EXAKT 400) with

polishing paper (grain size P2500). The thicknesses of all slices were documented to span 140–470 μm.

For calibration purposes, a fifth dried and embedded bovine tooth was used to extract two pieces, one made of pure enamel and the other of pure dentin. The origin of the dentin piece was selected to be cut-out of material halfway between the pulp and the periphery, taken from a region just below the crown. The density of these samples was measured by weighing the pieces and by determining the volume using micro-CT (see next section), measured with voxel sizes of 10 $\mu m^3$. The determined values were: $\rho_D = 2.025 \pm 0.075$ g/cm$^3$ for dentin and $\rho_E = 2.75 \pm 0.05$ g/cm$^3$ for enamel.

## 6.6 | Slice imaging and density calibration

From the large number of slices produced, seven characteristic slices (crown and root cross-sections from T1–T3 + one central slice from T4) were tomographically imaged using an industrial EasyTom 150 S micro-CT scanner with 15 $\mu m^3$ voxel size (100 kV, 0.3 mm Cu filter, 2 avg, 1400 projections, CMOS framerate of 2 FPS). The two density-measured homogeneous samples of pure dentin and enamel were also measured along with the same parameters to serve during density calibration. The reconstructed micro-CT gray value data were converted into density values using these calibration samples ($\rho_D$ and $\rho_E$) and considering the density value of the acrylic glass slides ($\rho_S$) on which the tooth sections were mounted. A linear fit through the values derived from the main peaks visible in CT histograms yielded a calibration curve of $\rho = 0.75$ g/cm$^3$ $+ 3.8 \times 10^{-5}$g/cm$^3$ $\times$ (gray value).

## 6.7 | Micro-XRF measurements and quantification of sum spectra

Elemental mapping by micro-XRF was performed with a modified commercial spectrometer (M4 Tornado Plus, Bruker Nano GmbH), which utilizes a rhodium microfocus X-ray tube, a polycapillary lens, and a silicon drift detector with a carbon-based light element window.[53] The lateral resolution (full width at half maximum) derived by a knife-edge scan at the Zn K fluorescence line energy (8.64 keV) is 22.5 μm. The measurements were acquired in air under ambient conditions and with a tube acceleration voltage of 50 kV and current of 1 mA. All bovine tooth slices were imaged in-plane with a lateral step size of 60 μm and a measurement time of 60 s per point. All maps were deconvolved using the software SpecFit.[54] The resulting elemental maps were visualized by the software ImageJ (v. 1.53q).

For quantification of elemental compositions, $n = 3$ slices from the three different crowns of teeth T1–T3 and $n = 3$ slices from the root regions of those teeth were used, with one additional longitudinal slice taken from T4.

The Zn K fluorescence intensity maps were treated as topological images in which isolines were traced manually, separating six areas of similar Zn intensity with respect to the pulp, as shown in Figure 4A. Entire spectra were averaged from points collected in these areas, resulting in six average spectra for each investigated slice (a total of $n = 42$ for seven slices). These spectra were converted into mass fractions using the proprietary evaluation package FPQ-Tools, developed by Bruker. This software uses a fundamental parameter approach based on the Sherman equation[30] to forward calculate full spectra—and takes into account effects such as continuum scattering and the detector response (including escape, shelf, and pile-up peaks). Spectra of samples of all thicknesses as well as layered systems with the relevant self-absorption effects can be simulated. Here, the background was modeled with a stripping background up to 12 keV (15 cycles) and calculated analytically for the high energy regions of each spectrum. Calibration of the spectrometer parameters (including solid angle of detection, detector efficiency, and optic parameters) was performed by measuring single-element reference samples as well as multi-element glass reference samples (Breitländer GmbH). The uncertainty of the quantification due to this calibration procedure is in the range of 5%.

The limited thickness of the tooth slices (140–470 μm) results in the possibility of excitation or fluorescence radiation being transmitted to and from the underlying acrylic glass slides. Therefore, as sample model, a layered system was assumed with the dentin slices situated above plexiglass. The plexiglass slides, of known composition, were modelled as $C_5O_2H_8$ (8% H, 60% C, 32% O) and had a thickness of 2 mm and a density of $\rho_S = 1.18$ g/cm$^3$.

For the dentin slices (Section 2.3), the thickness, the density, and the dark matrix (which comprises elements not detectable in our micro-XRF spectra, due to limitations in excitation and detection) are necessary input parameters. The thickness of the individual slices was measured, see above. For the assignment of the components of the dark matrix, values from a previous publication were used,[55] because the bovine tooth samples originated from the same source. As explained elsewhere (see Bauer et al.[55]), the dark matrix (light elements C, N, H, and O) has an impact on quantification of all elements in the micro-XRF measurements. Therefore, to reach quantitative concentrations of Ca, P, and Zn in the present work, dark matrix values of 2.2% for H, 5% for N, 35% for O, 16% for C, 1.2% for Na, and 1.2% for Mg were inserted in the quantification procedure. When changing the fixed ratios of the dark matrix elements in the quantification, maximum uncertainties

can be estimated. When changing the concentration values of the dark matrix within their uncertainties,[29] variations of 4% for P, 6% for Ca, and 9% for Zn were obtained for an example sum spectrum on T4 (see Supporting Information, Section 5). Therefore, 10% uncertainty can be considered the upper limit for all quantification values presented here.

We also evaluated the impact of density variations on the quantification results by examining and multi-fitting the average spectra of the longitudinal slice of T4. Quantification of the six spectra in that slice was conducted both with a fixed mean density value for dentin ($\rho_D = 2.025 \pm 0.075$ g/cm$^3$) and also with variable density values derived from line profiles across the calibrated micro-CT data ($\rho_{D,i} = 2.1$, 2.1, 2, 1.92, 1.88, and 1.82 g/cm$^3$ for spectra 1–6, see Figure 3). When comparing the difference between the use of a mean density versus gradually varying density for determining mass fractions of Zn, Ca, and P, the difference observed was <1%, implying that differences of ~10% density have negligible impact on the quantification of concentrations of the main dentin elements, see Supporting Information. Therefore, for the purpose of all further micro-XRF quantification of Ca, P, and Zn, the fixed mean density $\rho_D$ was used.

## 6.8 | Alignment of micro-XRF and CT data

Image registration was used to align and match the micro-XRF with the micro-CT 3D data. Some micro-XRF slices at the edges of the teeth were omitted due to enhanced geometry effects of the curved outer surface. The following workflow was applied to the rest.

Initially, all CT images (125 or 24 μm/px) were interpolated/binned to match the pixel sizes of the micro-XRF measurements (60 μm/px). Both, the micro-CT as well as the Ca K distributions of the micro-XRF data were segmented into binary masks to separate the tooth slice from background. For the segmentation, different methods were used depending on the image quality: global threshold, Otsu threshold, and Gaussian mixture model (for details, see Supporting Information, Section 6). As a result, for each tooth a 3D CT data set of binary masked data and several 2D micro-XRF data sets of binary masked data were available. Thereafter, the CT data were rotated in 3D to match the micro-XRF slices plane assuming that the cutting process delivers parallel slices. The resulting rotated CT stack was used for alignment and further processing explained briefly in the following.

For registration of the micro-XRF data to micro-CT, the first micro-XRF slice was compared to all micro-CT slices using a rigid template-matching custom written python code. The algorithm searches for the best match in ($x$, $y$, $z$, $\theta$) with $\theta$ defined as the rotation of the micro-XRF slices in the $xy$-plane. Optimal matching is found when the error value $R(x, y, z, \theta)$ is minimized. This is repeated for all other micro-XRF slices with the boundary condition that an iteration through the micro-CT model can only start from a CT slice that is above the last matched CT location. The output was the best match of each micro-XRF measurement to the 3D CT data cube.

## 6.9 | Figures and visualization

All graphs were prepared with OriginPro 2021b and all pixel images with Fiji/Image J 1.53q. Microsoft Powerpoint 2013 was used for figure composition and schematic drawings.

### ACKNOWLEDGMENTS

This work was funded by the Deutsche Forschungsgemeinschaft (German Research Foundation) [project numbers 443841418 (IXdent) and 396127899 (FOR2804 InterDent—TP1)]. PZ is grateful for DFG professorship funding through FOR2804 TPZ. The authors would like to thank Fabian Nitsche and Dimitrijs Docenko from the FPQ team of Bruker AXS and Hamza Elfarraj for the micro-CT measurement of the reference samples for dentin and enamel. We thank the Helmholtz-Zentrum Berlin für Materialien und Energie for the allocation of synchrotron radiation beamtime. We thank Ivo Zizak for his help with micro-X-ray diffraction data collection at the mySpot beamline of BESSY II and Holger Kropf for assistance with the FIB-SEM instrument.

Open access funding enabled and organized by Projekt DEAL.

### CONFLICT OF INTEREST STATEMENT

The authors declare they have no conflict of interest.

### DATA AVAILABILITY STATEMENT

The data that support the findings of this study are available from the corresponding author upon reasonable request.

### ORCID

*Ioanna Mantouvalou* https://orcid.org/0000-0002-9696-2970

### REFERENCES

1. N. Reznikov, R. Shahar, S. Weiner, *Acta Biomater.* **2014**, *10*, 3815.
2. P. Fratzl, R. Weinkamer, *Prog. Mater. Sci.* **2007**, *52*, 1263.
3. J. D. Currey, R. Shahar, *J. Struct. Biol.* **2013**, *183*, 107.
4. K. Sauer, A. Silveira, V. Schoeppler, A. Rack, I. Zizak, A. Pacureanu, N. Nassif, I. Mantouvalou, W. de Nolf, C. Fleck, R. Shahar, P. Zaslansky, *Acta Biomater.* **2024**, *179*, 164.

5. A. Silveira, A. Davydok, C. Krywka, M. Scheel, T. Weitkamp, C. Fleck, R. Shahar, P. Zaslansky, *Adv. Sci.* **2025**, *12*, 2410617.
6. S. Weiner, R. Shahar, *Acta Biomater.* **2024**, *179*, 1.
7. P. W. Lucas, *Dental Functional Morphology: How Teeth Work*, Cambridge University Press, Cambridge **2004**.
8. R. Z. Wang, S. Weiner, *J. Biomech.* **1998**, *31*, 135.
9. J. H. Kinney, S. J. Marshall, G. W. Marshall, *Crit. Rev. Oral Biol. Med.* **2003**, *14*, 13.
10. R. Garberoglio, M. Brännström, *Arch. Oral Biol.* **1976**, *21*, 355.
11. *Ten Cate's Oral Histology: Development, Structure, and Function* (Ed: A. Nanci), Elsevier **2024**.
12. M. Robin, C. Djediat, A. Bardouil, N. Baccile, C. Chareyron, I. Zizak, P. Fratzl, M. Selmane, B. Haye, I. Genois, J.-M. Krafft, G. Costentin, T. Azaïs, F. Artzner, M.-M. Giraud-Guille, P. Zaslansky, N. Nassif, *Adv. Sci.* **2024**, *11*, 2304454.
13. N. Shuhaibar, A. R. Hand, M. Terasaki, *Anat. Rec.* **2021**, *304*, 1820.
14. O. W. Reeder, R. E. Walton, M. J. Livingston, D. H. Pashley, *J. Dent. Res.* **1978**, *57*, 187.
15. C. Chou, M. Kang, D. Y. Parkinson, R. Sulyanto, S. P. Ho, *Dent. Mater.* **2025**, *41*, 1167.
16. K.-W. Lee, H.-H. Son, M. Yoshiyama, F. R. Tay, R. M. Carvalho, D. H. Pashley, *Am. J. Dent.* **2003**, *16*, 68A.
17. D. H. Pashley, R. M. Carvalho, *J. Dentistry* **1997**, *25*, 355.
18. M. Lin, Z. Y. Luo, B. F. Bai, F. Xu, T. J. Lu, *PLoS One* **2011**, *6*, e18068.
19. A. Aminoshariae, J. C. Kulild, *J. Endod.* **2021**, *47*, 1696.
20. M. Khatibi Shahidi, J. Krivanek, N. Kaukua, P. Ernfors, L. Hladik, V. Kostal, S. Masich, A. Hampl, V. Chubanov, T. Gudermann, R. A. Romanov, T. Harkany, I. Adameyko, K. Fried, *J. Dent. Res.* **2015**, *94*, 945.
21. J. D. Currey, *J. Biomech.* **1969**, *2*, 477.
22. A. C. Deymier-Black, A. Veis, Z. Cai, S. R. Stock, *Scanning* **2014**, *36*, 231.
23. A. E. W. Miles, *Structural and Chemical Organization of Teeth*, Academic Press **1967**.
24. F. Brudevold, L. T. Steadman, M. A. Spinelli, B. H. Amdur, P. Grøn, *Arch. Oral Biol.* **1963**, *8*, 135.
25. R. M. Frank, M. L. Sargentini-Maier, J. C. Turlot, M. J. F. Leroy, *Arch. Oral Biol.* **1989**, *34*, 593.
26. W. M. G. Parker, J. W. Adams, D. P. Hocking, E. M. G. Fitzgerald, G. Shaw, M. B. Renfree, A. R. Evans, *Biol. Trace Elem. Res.* **2025**, *203*, 4607.
27. S. I. Djomehri, S. Candell, T. Case, A. Browning, G. W. Marshall, W. Yun, S. H. Lau, S. Webb, S. P. Ho, *PLoS One* **2015**, *10*, e0121611.
28. *Handbook of Practical X-Ray Fluorescence Analysis* (Eds: B. Beckhoff, B. Kanngießer, N. Langhoff, R. Wedell, H. Wolff), Springer Science & Business Media **2007**.
29. L. J. Bauer, H. A. Mustafa, P. Zaslansky, I. Mantouvalou, *Acta Biomater.* **2020**, *109*, 142.
30. J. Sherman, *Spectrochim. Acta* **1955**, *7*, 283.
31. M. Haschke, S. Boehm, *Advances in Imaging and Electron Physics*, Elsevier **2017**, 1.
32. S. Amarie, P. Zaslansky, Y. Kajihara, E. Griesshaber, W. W. Schmahl, F. Keilmann, *Beilstein J. Nanotechnol.* **2012**, *3*, 312.
33. B. K. B. Berkovitz, G. R. Holland, B. J. Moxham, *Oral Anat Histol Embryol*, Elsevier **2017**.
34. I. Zanette, B. Enders, M. Dierolf, P. Thibault, R. Gradl, A. Diaz, M. Guizar-Sicairos, A. Menzel, F. Pfeiffer, P. Zaslansky, *Sci. Rep.* **2015**, *5*, 9210.
35. F. Kabartai, T. Hoffmann, C. Hannig, *Med. Hypoth.* **2015**, *85*, 887.
36. G. H. Yassen, J. A. Platt, A. T. Hara, *J. Oral Sci.* **2011**, *53*, 273.
37. M. T. Rahman, A. Hossain, C. H. Pin, N. A. Yahya, *Biol. Trace Elem. Res.* **2019**, *187*, 51.
38. J.-B. Forien, I. Zizak, C. Fleck, A. Petersen, P. Fratzl, E. Zolotoyabko, P. Zaslansky, *Chem. Mater.* **2016**, *28*, 3416.
39. S. Wong, A. Eaton, C. Krywka, A. Nair, C. Drouet, A. Deymier, *J. Mech. Behav. Biomed. Mater.* **2025**, *166*, 106962.
40. B. Wingender, M. Azuma, C. Krywka, P. Zaslansky, J. Boyle, A. Deymier, *Acta Biomater.* **2021**, *122*, 377.
41. J.-B. Forien, C. Fleck, C. Krywka, E. Zolotoyabko, P. Zaslansky, *J. Mech. Behav. Biomed. Mater.* **2015**, *50*, 171.
42. M. C. Dean, J. Garrevoet, S. J. M. Van Malderen, F. Santos, M. Mirazón Lahr, R. Foley, A. Le Cabec, *Biology* **2023**, *12*, 1455.
43. S. R. Stock, A. Veis, A. Telser, Z. Cai, *J. Struct. Biol.* **2011**, *176*, 203.
44. J. R. Dorvee, A. Deymier-Black, L. Gerkowicz, A. Veis, *Connect. Tissue Res.* **2014**, *55*, 9.
45. R. He, C. Chou, L. Chen, M. Stoller, M. Kang, S. P. Ho, *Front. Dent. Med.* **2022**, *3*, 883336.
46. A. Togari, S. Arakawa, M. Arai, S. Matsumoto, *Gen. Pharmacol. Vasc. Syst.* **1993**, *24*, 1133.
47. H. H. Harris, S. Vogt, H. Eastgate, P. A. Lay, *J. Biol. Inorg. Chem.* **2008**, *13*, 303.
48. K. Moriwaki, Y. Shimpuku, S. Furuyama, *Radioisotopes* **1999**, *48*, 172.
49. R. M. Sulyanto, M. Kang, S. Srirangapatanam, M. Berger, F. Candamo, Y. Wang, J. R. Dickson, M. W. Ng, S. P. Ho, *J. Dent. Res.* **2021**, *100*, 1099.
50. C. O. S. Sorzano, F. de Isidro-Gómez, E. Fernández-Giménez, D. Herreros, S. Marco, J. M. Carazo, C. Messaoudi, *J. Struct. Biol. X* **2020**, *4*, 100037.
51. T. Weitkamp, D. Haas, D. Wegrzynek, A. Rack, *J. Synchrotron Radiat.* **2011**, *18*, 617.
52. H. Shemesh, T. Lindtner, C. A. Portoles, P. Zaslansky, *J. Endod.* **2018**, *44*, 120.
53. T. Lachmann, G. van der Snickt, M. Haschke, I. Mantouvalou, *J. Anal. At. Spectrom.* **2016**, *31*, 1989.
54. F. Förste, L. Bauer, K. Heimler, B. Hansel, C. Vogt, B. Kanngießer, I. Mantouvalou, *J. Anal. At. Spectrom.* **2022**, *37*, 1687.
55. L. J. Bauer, F. Wieder, V. Truong, F. Förste, Y. Wagener, A. Jonas, S. Praetz, C. Schlesiger, A. Kupsch, B. R. Müller, B. Kanngießer, P. Zaslansky, I. Mantouvalou, *Anal. Chem.* **2024**, *96*, 8441.


## SUPPORTING INFORMATION

Additional supporting information can be found online in the Supporting Information section at the end of this article.

**How to cite this article:** I. Mantouvalou, L. J. Bauer, V.-B. Truong, Y. Wagener, F. Förste, O. Marushchenko, S. Werner, F. Lizzi, F. Wieder, T. Wolff, B. Kanngießer, P. Zaslansky, *VIEW.* **2026**, 20250173. https://doi.org/10.1002/VIW.20250173